The Meteoritical Society

Meteoritics & Planetary Science 51, Nr 4, 743–756 (2016)
doi: 10.1111/maps.12620

Microstructural analysis of Wark-Lovering rims in the Allende and Axtell CV3 chondrites: Implications for high-temperature nebular processes

Diana BOLSER[1], Thomas J. ZEGA[2,3*], Abu ASADUZZAMAN[3], Stefan BRINGUIER[3], Steven B. SIMON[4], Lawrence GROSSMAN[4], Michelle S. THOMPSON[2], and Kenneth J. DOMANIK[2]

[1]Department of Chemistry and Biochemistry, University of Arizona, Tucson, Arizona 85721, USA
[2]Lunar and Planetary Laboratory, Department of Planetary Sciences, University of Arizona, Tucson, Arizona 85721, USA
[3]Department of Materials Science & Engineering, University of Arizona, Tucson, Arizona 85721, USA
[4]Department of Geophysical Sciences, University of Chicago, Chicago, Illinois 60637, USA
[*]Corresponding author. E-mail: tzega@lpl.arizona.edu

(Received 05 May 2015; revision accepted 13 January 2016)

Abstract–A coordinated, electron-backscatter-diffraction (EBSD) and transmission electron microscope (TEM) study was undertaken to obtain information on the origin of rims on refractory inclusions in the Allende and Axtell CV3 chondrites. These measurements were supported by theoretical modeling using density functional theory. Crystal-orientation analysis of Wark-Lovering rims via EBSD revealed pyroxene grains with similar crystallographic orientations to one another in both inclusions. An epitaxial relationship between grains within the diopside and anorthite rim layers was observed in Allende. TEM examination of the rims of both samples also revealed oriented crystals at depth. The microstructural data on the rims suggest that grain clusters grew in the form of three-dimensional islands. Density functional theory calculations confirm that formation of oriented grain islands is the result of energy minimization at high temperature. The results point toward condensation as the mode of origin for the rims studied here.

INTRODUCTION

Calcium-aluminum-rich inclusions (CAIs) are mm- to cm-sized objects that occur in chondritic meteorites and are composed of refractory mineral phases that formed at very high temperatures. These phases are predicted by thermodynamic models to be among the first solids to condense from a cooling gas of solar composition (Grossman 1972; Ebel and Grossman 2000; Lodders 2003; Ebel 2006), so they can provide insights into the chemistry of the early solar system. Surrounding many CAIs are multilayered shells called Wark-Lovering rims, hereafter referred to as 'rims' (Wark and Lovering 1977). Several mechanisms for rim formation have been proposed including condensation, metasomatic exchange, and flash heating (MacPherson et al. 1981; MacPherson and Grossman 1984; Davis et al. 1986; Davis and MacPherson 1994; Krot et al. 1995; Wark and Boynton 2001; MacPherson 2004).

CAI types include irregularly shaped fluffy type A (FTA) inclusions, rounded compact type A (CTA) inclusions, and igneous type B inclusions. MacPherson and Grossman (1984) described FTAs as containing Al-rich melilite, V-rich spinel, perovskite, and hibonite that likely formed by condensation in the early solar nebula. The CTA inclusions were recognized by MacPherson and Grossman (1979) as having spheroidal shapes and zoned Mg-rich melilite. It is generally believed that most CTAs crystallized from melts, based on fractional crystallization models (Simon et al. 1999) and dynamic crystallization experiments on synthetic analogs (Beckett et al. 2006). Type B inclusions are also believed to have crystallized from liquids formed by partial melting of pre-existing solids (Blander and Fuchs 1975; Stolper and Paque 1986). Another abundant family of CAIs is the fine-grained spinel-rich inclusions found in CV chondrites. These inclusions range from heavily altered and highly porous to compact with little alteration. The

inclusions have an internal structure composed of monomineralic layers, and trace element signatures that imply they are a product of reactions between solids and nebular gas (Huss et al. 2002; Krot et al. 2004).

The optical microscope and electron and ion microprobes have been used extensively to study the properties of CAIs and have provided a wealth of information on their origins (e.g., Grossman 1975; Allen et al. 1978; Armstrong et al. 1982; MacPherson et al. 1983; Kornacki and Wood 1984; Ireland 1988; Simon et al. 1994; Krot et al. 1995). In comparison, there are fewer studies that have investigated the crystal chemistry and structure of CAI minerals, but these have provided valuable glimpses into their complex microstuctures (Doukhan et al. 1991; Greshake et al. 1998). For example, Barber et al. (1984) examined the microstructure of CAIs from the Allende CV3 chondrite via transmission electron microscopy (TEM) and concluded that formation occurred under conditions close to equilibrium through slow cooling and postcrystallization effects of solid-state diffusion. Hydration of CAI phases was also examined by TEM and evidence for parent-body and nebular alteration was identified (Keller and Buseck 1991; Greenwood et al. 1994).

The advent of focused ion beam (FIB)-enabled TEM studies provided a new way of gaining insights into site-specific components of meteorites (Stroud et al. 2000; Heaney et al. 2001; Lee et al. 2003), including CAIs. Particularly, the high current and focused Ga^+ probe of modern field-emission FIBs, combined with in situ micromanipulators, overcame the limitations posed by conventional Ar-ion milling techniques (Zega et al. 2007a; Graham et al. 2008). With FIB-SEM, radiation-hard materials, such as those that occur within CAIs and rims, can be site-specifically extracted and ion-milled to electron transparency. The FIB-SEM approach has been used to investigate a variety of planetary materials, such as meteorites, interplanetary dust particles, and presolar grains, and to guide sampling of individual objects for multiple analytical studies (e.g., Stroud et al. 2004; Zega et al. 2014; Busemann et al. 2009; Floss et al. 2014; Nguyen et al. 2010).

Here we build on earlier efforts aimed at understanding the detailed microstructural features of CAIs (Toppani et al. 2006; Zega et al. 2007b, 2009, 2010; Paque et al. 2009; Ma et al. 2011; Keller et al. 2013, 2014; Han et al. 2014, 2015a, 2015b). We apply electron-backscatter-diffraction (EBSD) and TEM enabled by FIB-SEM to the analysis of rims in a CTA from Axtell and an FTA from Allende. There are a number of important observations that are now routinely available from EBSD analysis but are not obtainable from conventional methods of microstructural characterization. These include local relationships between microstructure and grain orientations as well as information on grain and phase boundaries. The goal of combining EBSD and TEM studies in this work is to obtain coordinated three-dimensional crystallographic information about rims on CAIs in order to gain new insights into their formation and evolution.

SAMPLES AND METHODOLOGY

We investigated a CTA identified in a thin section of Axtell (AX30, Field Museum) and an FTA identified in a thin section of Allende (TS25, U. Chicago). Axtell and Allende are both members of the oxidized subgroup of CV3 chondrites (McSween 1977). These samples were chosen in order to compare the crystallographic features of rims on previously molten refractory inclusions (CTAs) to those that are believed to have condensed from the nebular gas (FTAs). We used a Cameca SX-100 electron microprobe at the Lunar and Planetary Laboratory (University of Arizona) to obtain backscattered electron (BSE) images that were stitched together to form mosaics of the entire thin sections for use in selection of specific sites for detailed analysis using EBSD and TEM. The compositions of rim layers in Allende were also measured with the Cameca SX-100 electron microprobe using a focused (~1 μm) beam operated at 15 kV and 20 nA. Counting times were 20 s on peak and 20 s on background and PAP matrix corrections were applied for each analysis. Wavelength-dispersive spectrometers were calibrated using well-characterized natural minerals and materials. Oxygen concentration was calculated by stoichiometry.

In order to obtain highly polished surfaces appropriate for EBSD measurement, the thin sections were polished using 1 μm diamond paste followed by 0.05 μm colloidal silica on an automatic VibroMet 2 Vibratory Polisher for a minimum of 3 h. After polishing, samples were coated with a thin layer of carbon to avoid surface charging during microbeam imaging and analysis. EBSD data acquisition was carried out on a Hitachi 3400N SEM equipped with an Oxford EDS/EBSD system. An accelerating voltage of 20 kV and an approximate incident beam current of 3.75 nA were used. The stage was positioned at a 70° tilt from the horizontal. The Kikuchi diffraction patterns were indexed automatically in real time and the results were analyzed using HKL Channel 5 software. Pattern-quality and Euler-orientation maps were constructed with a 500 nm step size and a dwell time of 0.5 s.

For each CAI, one area of roughly 100 × 100 μm, containing several thousand individual grains ranging in size from 0.5 to tens of microns across, was analyzed by EBSD. For the purposes of this study, only grains from the rim are discussed, although the maps also contain grains from the matrix and interior of the CAI. Data were corrected by replacing pixels with zero solutions with the most common orientation among seven neighbors followed by elimination of wild spikes (wrongly indexed pixels). Clustering, where grains have orientations within 5° of one another, was used to improve efficiency of data processing.

To visualize grain orientations, the data were plotted on an equal-area upper-hemisphere pole-figure plot, and the degree to which the pole is spread out over the projected sphere was controlled with a half-width value of 10°. The crystallographic orientations are displayed as pole figures, which map a selected set of crystal plane normals plotted with respect to the specimen reference frame. Thus, an {*hkl*} pole figure shows the distribution of the *hkl* poles in the sample. The intersection of the crosshairs of the pole figure represents the surface perpendicular to the specimen. Pole figures express the probability of finding a lattice plane in a certain sample direction in multiples of uniform density (m.u.d.). A m.u.d. of one indicates randomly oriented grains; a m.u.d. greater than one is indicative of a preferred orientation. Grain orientations are given in terms of Euler angles, which relate the orientation of individual grains to the sample coordinate system. For orientation maps, we assign false colors generated by the superposition of three color channels (red, green, and blue), which are correlated with the values of the three Euler angles (ϕ_1, Φ, ϕ_2) of each measured pixel. Therefore, similar colors represent similar grain orientations.

Following broad-scale EBSD measurements, we selected specific sites for detailed analysis at depth using TEM. Sites were chosen based on where EBSD revealed the presence of a preferred crystallographic orientation on the surface. The regions were extracted and thinned to electron transparency with an FEI Nova 200 FIB-SEM at Arizona State University and an FEI Quanta 3D FIB-SEM at NASA Johnson Space Center using previously described techniques (Zega et al. 2007a, 2007b). The FIB sections were analyzed with a 200 keV JEOL 2010F TEM equipped with an EDAX energy-dispersive X-ray spectrometer (EDS) located at Arizona State University and a 200 keV JEOL 2500SE TEM at NASA JSC equipped with a ThermoNoran EDS and both STEM-based bright-field (BF) and dark-field (DF) detectors. Mineral structure was determined using selected-area electron-diffraction (SAED) patterns. All SAED patterns were measured with the crystallographic image processing software (CRISP) package based on calibrated camera constants and indexed to the appropriate reference structures.

Density functional theory (DFT) calculations were performed in order to model the atomic structures of the layers and examine the energy-minimized interfaces among them. Calculations were performed using the Vienna ab-initio simulation package version 5.2 (Kresse and Furthmuller 1996; Kresse and Joubert 1999). The exchange-correlation contribution to the total energy is modeled using the generalized gradient approximation of Perdew–Burke–Ernzerhof (PBE; Perdew et al. 1996). Electronic interactions were described by the projected augmented wave method (Blöchl 1994). The cutoff energy for the plane wave expansion is set to 400 eV. The surface and interface were modeled using a periodic supercell. A periodic supercell was constructed from smaller diopside and anorthite unit cells in order to model the surfaces and interface between them. Each surface is separated by a vacuum space of 15 Å to prevent spurious interactions between them. A convergence criterion that ensures all atomic forces are smaller than 0.02 eV/Å was imposed while locating energy-minimized surfaces.

RESULTS

Petrography and Mineralogy

Axtell inclusion AX30 is a CTA that consists primarily of melilite with minor perovskite and spinel (Fig. 1). As is typical for CTAs, melilite compositions in AX30 have a range of $Åk_{15–35}$ and an average composition of $Åk_{23}$ (Simon et al. 1999), except for relatively gehlenitic melilite ($Åk_{8–20}$) that occurs in the outermost ~10 μm, just inside the Wark-Lovering rim. A rim sequence (40–50 μm) surrounds the entire inclusion and consists of an outermost, continuous layer of pyroxene overlying a layer of spinel intergrown with perovskite. While many rims have complex, multilayer structures, the AX30 rim studied in this investigation is composed of an outer pyroxene layer and an inner spinel/perovskite layer. The results presented here pertain to the pyroxene layer. Mg-Al spinel contains minor Ti (0.5 wt%) and perovskite contains minor V (0.1–0.2 wt%). Pyroxene is Mg- and Ca-rich, with MgO wt% ranging from 13.71 to 17.20 and CaO wt% ranging from 24.82 to 25.81. The pyroxene TiO_2 contents range from 0.48 to 2.52 wt%, decreasing outward from the inclusion (Table 1).

Allende TS25 is an FTA that consists of large, reversely zoned melilite ($Ak_{20–10}$) crystals with inclusions of spinel, hibonite, and perovskite (Fig. 2). It has an irregular, nodular shape and each nodule has a rim, so

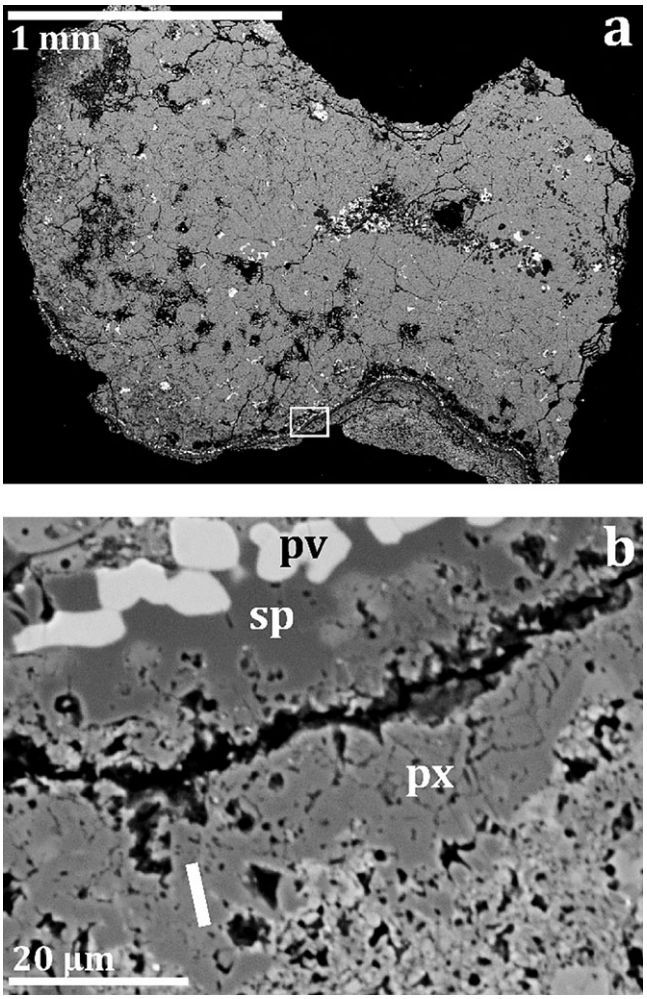

Fig. 1. Backscattered electron images of compact type A CAI AX30. a) View of the entire section. b) A region of interest for EBSD analysis from the area indicated in (a). The W-L rim consists of perovskite (pv), spinel (sp), and pyroxene (px). The white bar indicates the location where a FIB section was extracted for TEM analysis.

regions of interest relevant to the present study can be found in the apparent interior of the inclusion (Fig. 2b). This inclusion was described in detail by MacPherson and Grossman (1984) and Cosarinsky et al. (2008). The rim sequence (20–30 μm) consists of three distinct layers of stoichiometric spinel, anorthite, and Ti-rich pyroxene grading outward from the inclusion. Representative electron probe analyses are shown in Table 2. There are three distinct types of pyroxene present in the rim: high-Al pyroxene, which has Al_2O_3 contents averaging 3.28 wt%; low-Al pyroxene with Al_2O_3 contents averaging 0.86 wt%; and very abundant high-Al,-Ti pyroxene (fassaite) with inhomogeneous Al_2O_3 and TiO_2 contents averaging 12.83 and 5.60 wt%, respectively. The spinel grains have an Mg# of 0.99, and the anorthite composition averages $An_{99}Ab_{01}Or_0$.

Table 1. Representative electron microprobe analyses of perovskite (PV) and pyroxene (PX) in the rim of AX30.

	PV1	PV2	PX1	PX2	PX3
SiO_2	0.12	0.15	46.97	50.34	51.15
TiO_2	56.71	57.55	2.52	1.05	0.48
Al_2O_3	0.58	0.66	10.10	5.07	5.27
Cr_2O_3	n.d.	n.d.	0.06	0.08	0.04
V_2O_3	0.09	0.09	0.09	0.08	0.03
FeO	0.20	0.16	1.07	1.62	0.32
MgO	0.06	0.08	13.71	15.54	17.20
CaO	40.67	40.35	25.13	24.82	25.81
SUM	98.45	99.04	99.65	98.60	100.30
Si	0.003	0.004	1.718	1.858	1.849
Ti	0.980	0.986	0.069	0.029	0.013
Al	0.016	0.018	0.436	0.220	0.225
Cr	n.d.	n.d.	0.002	0.002	0.001
V	0.002	0.002	0.003	0.002	0.001
Fe	0.004	0.003	0.033	0.050	0.010
Mg	0.002	0.003	0.747	0.855	0.927
Ca	1.001	0.985	0.985	0.982	1.000
Total	2.008	2.001	3.993	3.998	4.026

Oxides are in weight percent (wt%). Perovskite cations normalized to 3 oxygen anions, pyroxene cations normalized to 6 oxygen anions. Perovskite V_2O_3 contents have been corrected for interference from Ti. All Ti is reported as TiO_2.

EBSD Analysis of Rims

Crystal orientation and microstructure of pyroxene grains within the rims were investigated by EBSD. The focus is on pyroxene because it was previously reported that oriented pyroxene grains were found in rims on Allende and Vigarano inclusions (Zega et al. 2009, 2010). The Euler maps show a distribution of orientations within each of the CAIs. There are clusters of grains within individual rim layers that share common orientations and there are adjacent rim layers that share an orientational relationship.

In AX30, we measured a total of 3023 grains within one area of the rim. This represents a small part of the entire rim, but nonetheless captures a statistically significant sampling of grains. These grains range from 0.5 to 17 μm across, with the majority under 5 μm and only four grains over 10 μm. Of those 3023 grains, 1358 are pyroxene. The remaining grains are spinel, perovskite, and melilite. An extensive portion (575 grains or ~42%) of this region of the pyroxene layer consists of similarly oriented grains (Fig. 3a). These are represented on upper-hemisphere equal-area projections (Fig. 3b). Each pole figure has a single hot spot, indicating that this subset of grains is dominated by a single orientation. The distance of the hot spot relative to the crosshairs reflects the angular variation of the grains from the

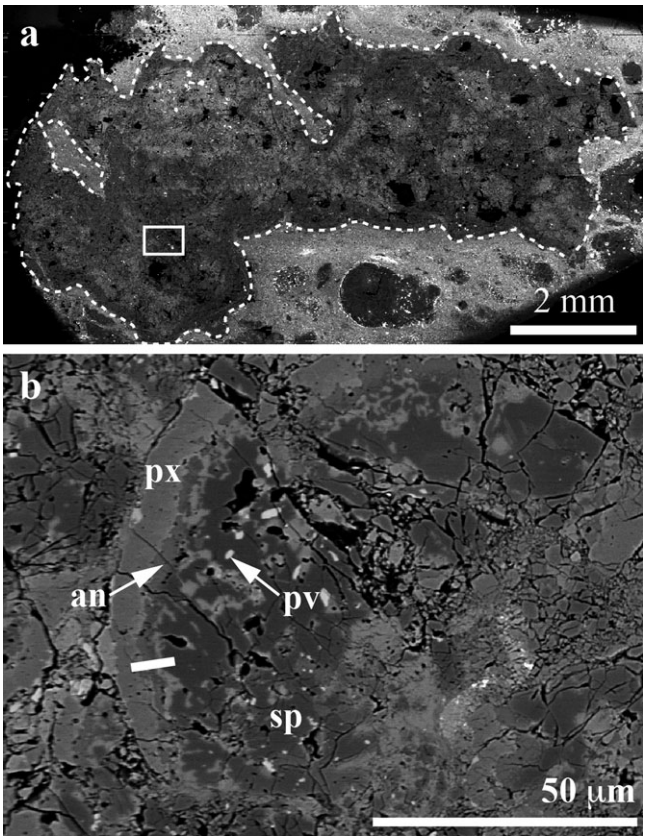

Fig. 2. Backscattered electron images of fluffy type A CAI TS25. a) View of the entire section. White-dashed line outlines the CAI. b) A region of interest for EBSD analysis from the area indicated in (a). The rim consists of perovskite (pv), spinel (sp), anorthite (an), and pyroxene (px). The white bar indicates the location where a FIB section was extracted for TEM analysis.

Table 2. Representative electron microprobe analyses of high-Al pyroxene (HAlPX), low-Al pyroxene (LAlPX), and high-Al-Ti pyroxene (AlTiPX), spinel (SP), and anorthite (AN) in the rim of TS25.

	HAlPX	LAlPX	AlTiPX	SP	AN
SiO_2	52.27	54.36	44.18	0.05	41.46
TiO_2	0.73	0.25	5.60	0.24	0.29
Cr_2O_3	0.05	0.04	0.05	0.12	n.d.
Al_2O_3	3.28	0.86	12.36	71.76	36.57
FeO	0.12	0.07	0.11	0.57	0.13
MnO	n.d.	n.d.	n.d.	n.d.	n.d.
MgO	17.75	18.49	12.54	27.40	0.76
CaO	25.24	25.48	25.36	0.09	19.79
Na_2O	0.05	n.d.	n.d.	n.d.	0.06
K_2O	n.d.	n.d.	n.d.	n.d.	n.d.
SUM	99.50	99.63	100.21	100.25	99.10
Si	1.899	1.969	1.609	0.001	1.945
Ti	0.020	0.007	0.154	0.004	0.010
Cr	0.001	0.001	0.001	0.002	n.d.
Al	0.141	0.037	0.532	2.003	2.022
Fe	0.004	0.002	0.003	0.011	0.005
Mn	n.d.	n.d.	n.d.	n.d.	n.d.
Mg	0.961	0.998	0.680	0.967	0.053
Ca	0.983	0.989	0.990	0.002	0.995
Na	0.004	n.d.	n.d.	n.d.	0.005
K	n.d.	n.d.	n.d.	n.d.	n.d.
Total	4.012	4.006	3.971	2.992	5.037

Oxides are in weight percent (wt%). Pyroxene cations normalized to 6 oxygen anions, spinel cations normalized to 4 oxygen anions, anorthite normalized to 8 oxygen anions. All Ti is reported as TiO_2.

specimen normal direction. Thus, the grains are oriented at 52° with respect to the {100} surface normal, 43° with respect to the {010} surface normal, and 45° with respect to the {001} surface normal.

In TS25, we measured a total of 8,082 grains within one area of the rim. These grains have equivalent diameters ranging from 0.5 to 12 μm with the majority under 3 μm and only two grains over 10 μm. Of those 8082 grains, 1569 are pyroxene. The remaining grains are spinel, hibonite, perovskite, and melilite. A portion (603 grains or ~38%) of the pyroxene layer consists of similarly oriented grains (Fig. 4a). The crystal orientations of the pyroxene grains are shown on the upper-hemisphere equal-area projections (Fig. 4b). Two hotspots occur, indicating grains are clustered at polar angles of 33° and 83° relative to the {100} pole; 75° and 36° relative to the {010} pole and 62° with respect to the {001} pole.

EBSD also shows that clusters of anorthite grains within the rim have similar orientations (Fig. 4c). Of the 8082 total grains, 112 are anorthite. Each pole figure has a single hot spot, indicating that this subset of anorthite grains is dominated by a single orientation. The anorthite grains cluster at 87° from the {100} pole and are thus nearly parallel to the surface of the thin section. Relative to the other two poles, the grains cluster at 67° relative to {010} and 60° relative to {001}.

TEM Cross Sectional Analysis

A TEM study of the rims in TS25 and AX30 was performed in order to characterize subsurface relationships and compare them with surface trends. FIB sections were extracted from areas where EBSD revealed the presence of grains with similar crystallographic orientations (see Figs. 1 and 2 for locations of transects). The FIB section of AX30 consists entirely of pyroxene (Fig. 5a). We acquired elemental X-ray maps and SAED patterns to verify the pyroxene composition and structure. Microprobe analysis of the pyroxene shows that it is Al- and Ca-rich $Ca(Mg_{0.6}Ti_{0.3}Al_{0.1})(Si_{1.3}Al_{0.7})O_6$. However, TEM-

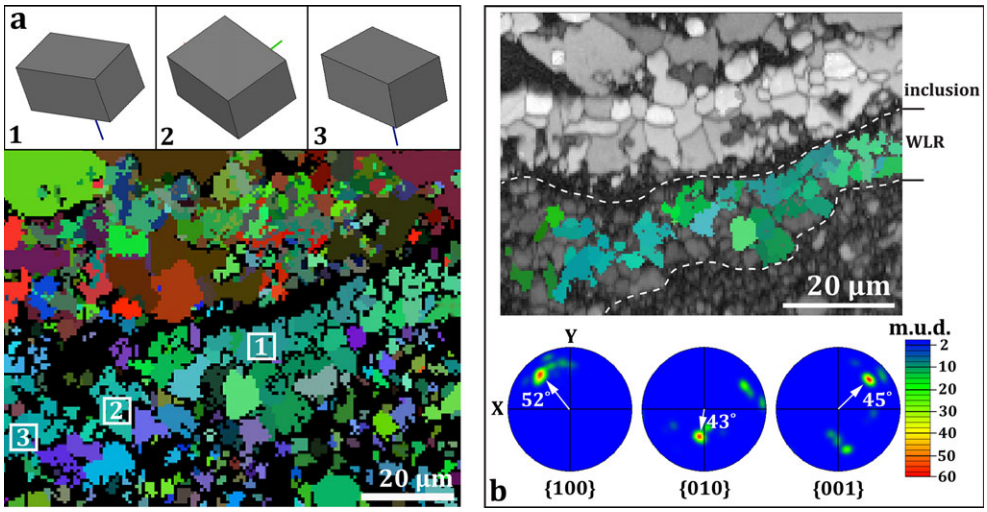

Fig. 3. EBSD data for AX30. a) Euler map showing the orientations of pyroxene crystals within the rim from the indicated locations. Orientations for select regions (1, 2, and 3) are shown in block form (top) with primary crystallographic axes indicated as green (*b*-axis) and blue (*c*-axis) lines. Similar colors in the map (bottom) indicate similar grain orientations. b) Grain contrast map of AX30 overlaid with Euler orientations of pyroxene. The {100}-, {010}-, and {001}-pole figures for the grains are shown below. Note the scale of m.u.d. values to the right of the pole figures. Clusters of grains with similar orientations plot as hotspots within the pole figures. The white arrows represent the angular deviations of the grains from the pole.

EDS mapping of part of the FIB section shows both Ca-rich and Ca-poor pyroxene occur below the surface. SAED patterns acquired from part of the FIB section indicate orthopyroxene (Figs. 5b and 5c).

In comparison, the FIB section of TS25 transects anorthite, Ti-rich pyroxene, and spinel as revealed by EDS maps (Figs. 6a–c). Standardless quantification of EDS spectra is consistent with a nominally stoichiometric anorthite ($Ca_{1.0}Al_{2.1}Si_{1.9}O_8$) composition. Spinel is $MgAl_2O_4$, with low concentrations (<0.5 wt%) of Ti (Fig. 6b) and Fe. Ti-rich pyroxene has a composition of $(Ca_{1.0}Mg_{0.6}Ti_{0.3})(Si_{1.5}Al_{0.5})O_6$ and it encloses spinel (Fig. 6b). Measurements of interplanar spacing and angles from SAED patterns acquired from multiple grains are consistent with anorthite [010] and diopside [13$\bar{4}$] structures (Figs. 6d–f). SAED patterns acquired from several areas show no angular variation among the diopside crystals (Figs. 6e and 6f). We note that the orientation of diopside crystals at depth is not necessarily identical to that on the surface because the view in cross section is shifted 90° from the surface.

Density Functional Theory Simulations

DFT simulations were used to gain further insight into the structure of the interface between diopside and anorthite layers in the rim of TS25. In order to construct a model of the interface, we generated diopside (13$\bar{4}$) and anorthite (010) surfaces from their respective crystalline phases based on the orientations of the crystals revealed by SAED patterns (Fig. 6). The interface was built by placing one surface on top of the other, and the structures were relaxed to their local energy minima (Fig. 7). We note that there is limited commensuration between the diopside and anorthite lattices, and as a consequence, the mismatch between the surfaces requires stretching the structures relative to each other by using the average of the lattice vectors of the two surfaces to generate the interface.

A thermodynamically stable interfacial structure was formed between diopside and anorthite only if the respective lattices were strained by 1.15–1.17% and 3.26–3.49% in the *a* and *b* directions, respectively. Based on the equation

$$\Delta E = E_{\mathrm{Int}} - E_{\mathrm{An}} - E_{\mathrm{Di}} \tag{1}$$

where E_{Int}, E_{An}, and E_{Di} are the total energy of interface structure, and anorthite and diopside surfaces, respectively, the interfacial energy was found to equal 5.39 eV for standard surfaces and −6.34 eV for strained surfaces. The fact that the respective lattices have to accommodate strain to enable an energetically stable interface implies either thermal or impact processes were active during interface formation.

The interface is characterized by ionic bonds formed between the electropositive and electronegative surface atoms of anorthite and diopside. Specifically, for diopside (13-4), the surface atoms are O, Ca, and Mg,

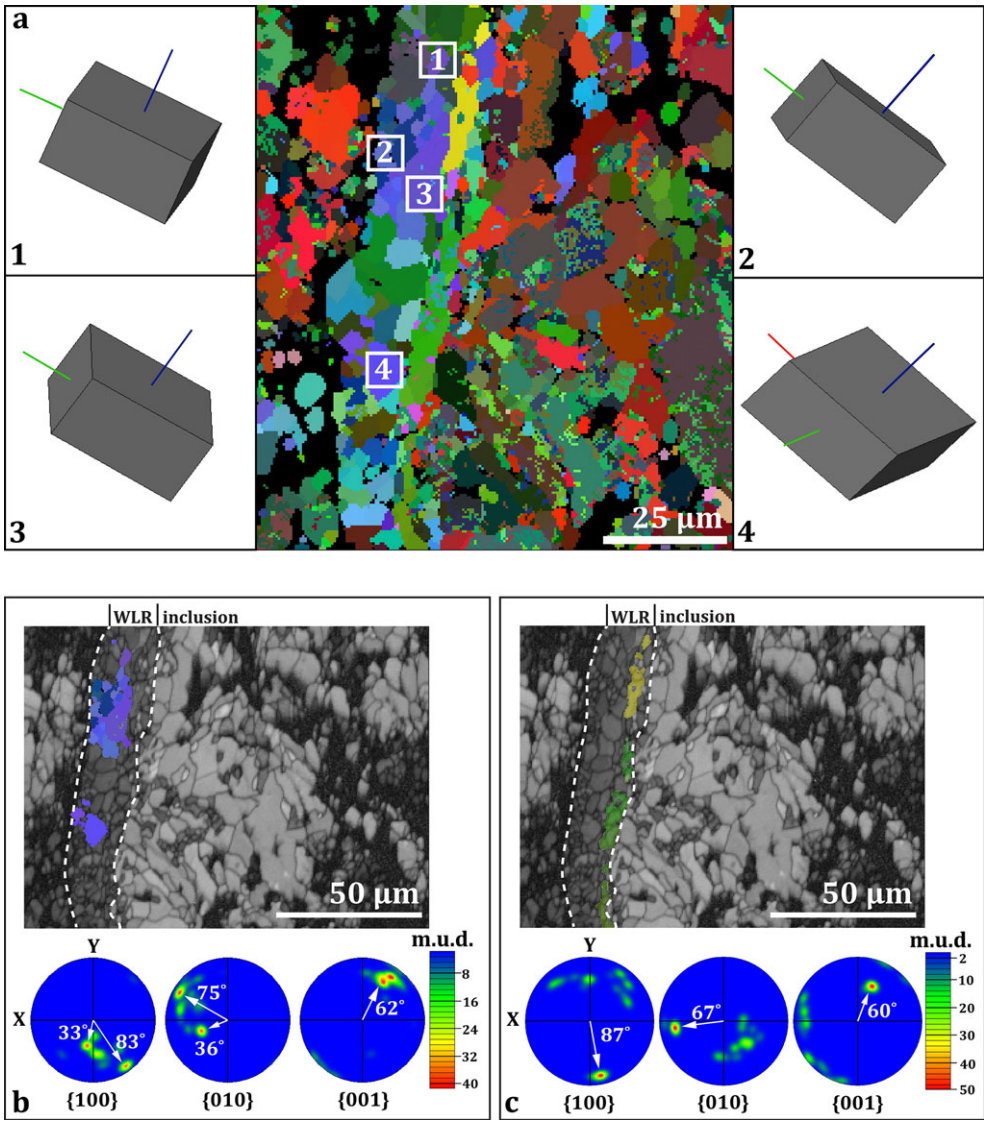

Fig. 4. EBSD data for TS25. a) Euler map showing the orientations of pyroxene crystals within the rim from the indicated locations. Primary crystallographic axes are indicated by red (*a*-axis), green (*b*-axis), and blue (*c*-axis) lines. Similar colors indicate similar grain orientations. b) Grain contrast map overlaid with Euler orientations of pyroxene. The {100}-, {010}-, and {001}-pole figures for the grains are shown below. The white arrows represent the angular deviations of the grains from the pole. c) Grain contrast map overlaid with Euler orientations of anorthite. The {100}-, {010}-, and {001}-pole figures for the grains are shown below. Clusters of grains with similar orientations plot as hotspots within the pole figures. The white arrows represent the angular distributions of the grains from the pole. The scale of m.u.d. values is to the right of the pole figures.

whereas for anorthite (010), the surface atoms are O and Ca (Fig. 7). While the anorthite and diopside lattices are strained parallel to the interface, there is no noticeable reconstruction normal to the interface, i.e., the interface and the bulk have the same structure.

DISCUSSION

The EBSD results show that there are clusters of grains within individual rim layers that share common orientations, and that adjacent layers share an orientational relationship. In addition, the analysis of FIB cross sections in the TEM reveals that diopside crystals below the surface have grown in orientations similar to one another, corroborating the trend observed on the surface through EBSD. This indicates that the same process that led to oriented grains extending across the surface of the CAI was active in three dimensions and led to the formation of clusters of grains at depth.

The density functional theory calculations show that the formation of a thermodynamically favorable

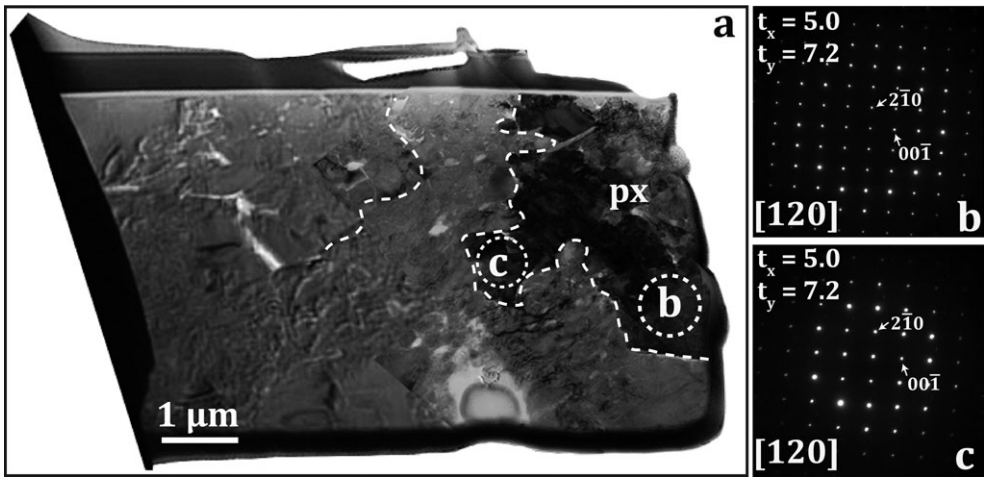

Fig. 5. TEM data on a FIB section of AX30 traversing the rim where EBSD detected the presence of a preferred orientation on the surface, as shown in Fig. 1b. a) BF- STEM image of a section composed of pyroxene (px). Dashed lines delineate grain boundaries. Note that the surface of the FIB section, which is the thin-section surface, is at the top of the image. b, c) SAED patterns of orthopyroxene [120] acquired from regions indicated by white-dashed circles in (a). Patterns b and c were acquired at the same goniometer tilt angles (t_x, t_y), in degrees.

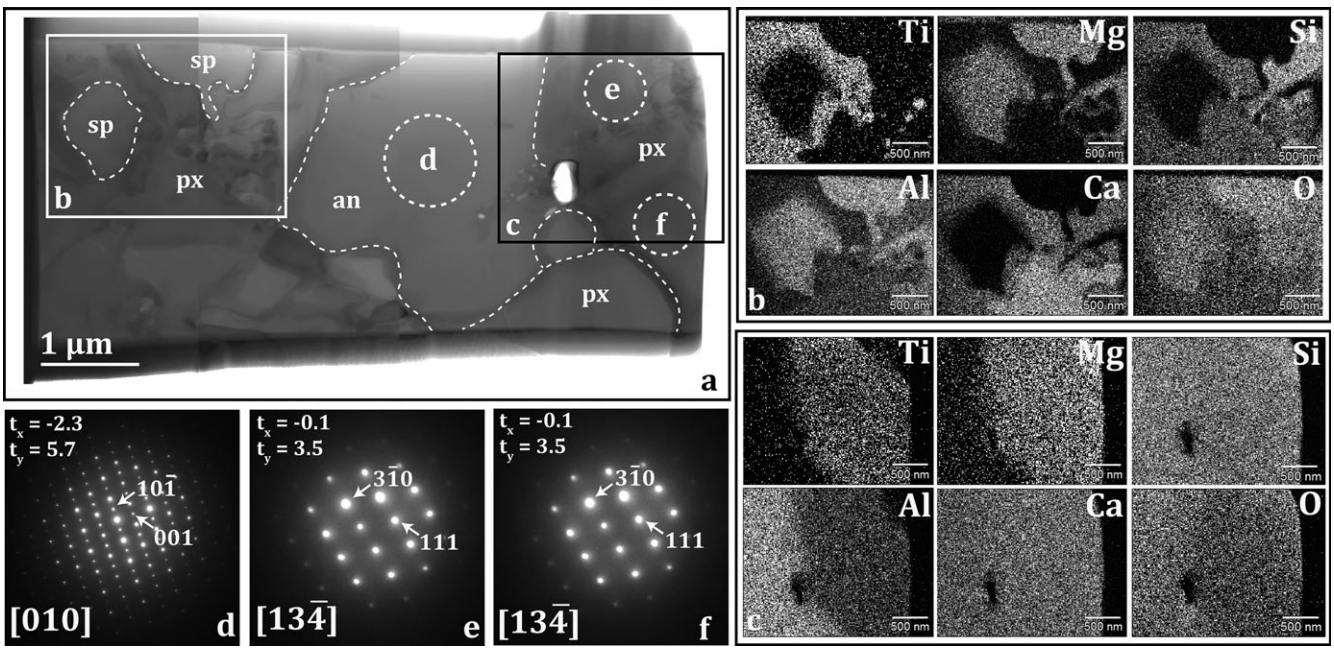

Fig. 6. TEM data on a FIB section of TS25 traversing the rim where EBSD detected the presence of a preferred orientation on the surface, as shown in Fig. 2b. a) BF-TEM image showing spinel (sp), anorthite (an), and pyroxene (px). Note that the surface of the FIB section, which is the thin-section surface, is at the top of the image. b, c) Elemental X-ray maps from regions outlined by rectangles in (a). Scale bars are 500 nm. d) SAED pattern of anorthite [010] acquired from region indicated by white-dashed circle in (a); e, f) SAED patterns of diopside $[13\bar{4}]$ acquired from regions indicated by white-dashed circles in (a). Patterns e and f were acquired at the same goniometer tilt angles (t_x, t_y), in degrees.

interface is due to the structural properties of the individual rim layers. The endothermic nature of interface formation between the diopside and anorthite standard surfaces can be understood based on the fact that there is a substantial angle mismatch (~10°) between them. When substantial mismatch between two different phases occurs, a coherent interface, i.e., one without defects between the two heterostructures, is highly unlikely to form. In the context of CAI and rim growth, this mismatch suggests that mechanical attachment, i.e., previously formed grains accreting to the surface, rather than chemical bonding, would be

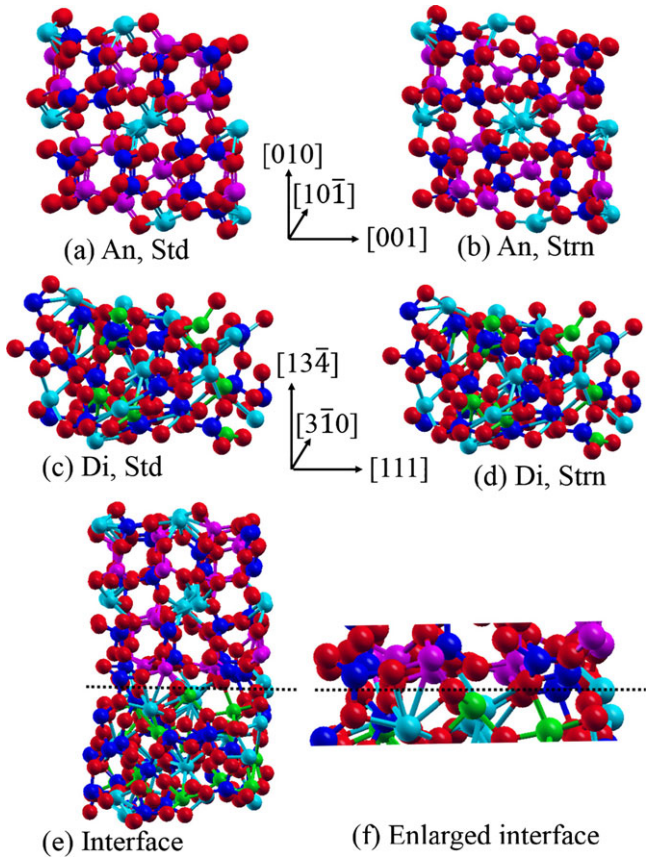

Fig. 7. Optimized surfaces for (a) standard ("Std") anorthite (010); (b) strained ("Strn") anorthite (010); (c) standard diopside (13$\bar{4}$); (d) strained diopside (13$\bar{4}$); and the (e) and (f) interface (marked by the dashed line). Note that in (e), the anorthite is oriented with [010] pointing upward, whereas the diopside is oriented with [13$\bar{4}$] upward. See text for discussion. Red, green, pink, blue, and cyan spheres represent O, Mg, Al, Si, and Ca atoms, respectively.

expected. However, the interface between diopside and anorthite is well defined and continuous in the BF-TEM image, for at least this part of the rim, i.e., it appears coherent. Such coherency suggests possible atomic registry, free of defects, between these heterostructures in this part of the rim in TS25 (Fig. 6a).

In comparison, when strained surfaces are used to calculate the energetics of the diopside [13$\bar{4}$]/anorthite [010] contact, interface formation becomes thermodynamically favorable. The calculated strain energies (Equation (1)) for anorthite and diopside are, respectively, 0.042 eV/atom and 0.024 eV/atom. The minimum temperatures needed (assuming no kinetic barrier) to form such a metastable surface are 487 and 278K, respectively (1 eV=11,605 K), for anorthite and diopside. These calculations therefore suggest a minimum temperature of 487K was required to form a stable interface from these two heterostructures. Given the high temperatures expected for condensation of rim phases (e.g., 1450K for diopside and 1326K for anorthite; Grossman 1972), it is plausible that such conditions could have led to the requisite shift in the lattice parameters of diopside and anorthite. The strained surfaces that would have resulted likely led to the coherent interface and therefore favored the growth of pyroxene on anorthite at elevated temperature for at least part of the TS25 rim observed here.

Based on the similar positions of hot spots in the diopside and anorthite pole figures (Figs. 4b and 4c), an orientational relationship must exist between these two phases in the TS25 rim. We hypothesize that grain nucleation began at pre-existing grain boundaries along directions controlled primarily by the structure of the melilite in the inclusion or the innermost rim layer. These surfaces acted as nucleation sites on which the rim phases condensed from the surrounding nebular gas, and this process is illustrated in Fig. 8. As growth proceeded, anorthite and diopside grains formed with similar orientations, producing island-type growth (described in more detail below). Ultimately, the islands merged together creating the observed microstructure (Fig. 8c). Coalescence of the grain clusters is likely controlled by a mechanism that favors preservation of similarly oriented grains and destroys strongly misoriented ones. The DFT calculations suggest that this process is driven by minimization of surface free energy. Specifically, the local condensing system can reduce its free energy by forming an interface from the strained surfaces as indicated by the calculated interface energy of −6.34 eV, which is energetically favorable.

The materials science community has long relied on island-growth models to describe the localized coalescence of atoms on a surface during vapor-phase thin-film growth. For example, Parker et al. (1999) described the vapor deposition of gold onto (110) planes of TiO_2 where coverage of Au islands increased with the defect density of the TiO_2 substrate. Also, Maranville et al. (2006) described the vapor deposition of $CoPt_3$ films in which island nucleation and growth occurred mostly on step edges. In the case of CAIs, the growth of islands would depend on the nature of the surfaces, e.g., defects and step edges, as well as the fraction of the atoms arriving at the surface of the CAI from the surrounding gas. Given the irregularity of the shapes of fluffy type A CAIs, like that of TS25, it seems likely that some amount of defects and step edges would occur and serve as nucleation sites for the first rim layer. Supporting evidence for the occurrence of such surface irregularities is provided by Muller and Wlotzka (1982), who reported melilite with high dislocation densities, and point defects in anorthite in the Leoville CV3 chondrite. Furthermore, Barber et al. (1984)

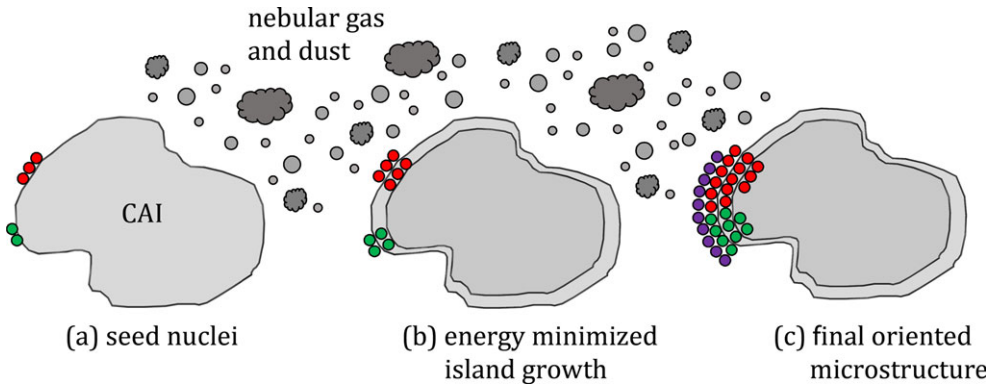

Fig. 8. Schematic model depicting rim growth whereby crystals condense in an oriented fashion onto the CAI surface in order to lower their surface free energy. a) Grain nucleation occurs when new crystals, represented by colored circles (same color indicates same orientation of a particular phase), form and orient themselves on pre-existing seed nuclei. b) Crystallization of the rim layers may have occurred at several different nucleation sites via an island-type growth mode. c) As material condensed from the nebular gas and dust and the rim grew in extent, these grain islands would have merged together, creating the observed microstructure.

reported high dislocation densities and considerable internal strain in melilite crystals in an FTA from Allende. Moreover, Zega et al. (2010) showed that grains within the spinel layer of a spinel–pyroxene rim surrounding Allende CAI (TS24) contain defects. These prior studies demonstrate that phases in CAI cores and those within their rims possess defect structures that could facilitate the subsequent nucleation of rim phases.

In hetero-epitaxial growth, there is mismatch between the lattice constants for the substrate and the deposited film (Hwang and Bartelt 1997; Shchukin and Bimberg 1999). For a large lattice mismatch, as is the case between diopside and anorthite, local structural disorder and excess energy lead to a prevalence of 3-D rather than 2-D islands (Evans et al. 2006), which correlates well with our experimental observations. EBSD revealed clusters of oriented grains extending over the surface of the thin section and TEM showed clusters of oriented grains below the surface, for both AX30 and TS25.

For AX30, the EBSD data reveal a preferred orientation among pyroxene grains within the rim. All the grains have approximately the same orientation and therefore cluster around a single hot spot. All three principal directions ({100}, {010}, and {001}) show clustering (Fig. 3b), suggesting that the measured grains nucleated together in situ rather than having undergone ex situ condensation from a gas followed by oriented attachment to the pre-existing melilite inclusion. If deposition of condensate grains had occurred, a uniform distribution of grain orientations within the rim would not be expected. Rather, if previously condensed grains had accreted to the surface of the melilite to make the rim, such grains would likely have done so in completely random orientations (and would not have produced coherent interfaces). TEM analysis also identified multiple pyroxene grains sharing the same [120] orientation (Figs. 5c and 5d), which shows that oriented growth occurs at depth. These data suggest that island-type growth also occurred in three dimensions for the pyroxene layer in AX30. We interpret the data in a similar way to TS25, with rim grains nucleating with similar orientations on pre-existing defects in an island-growth process. Defects in the melilite or spinel of AX30 could serve as nucleation sites. In a TEM study by Greshake et al. (1998), a high density of dislocations in melilite from CTAs in CV3 chondrites was described, which supports this hypothesis.

Cosmochemical Implications

Hypotheses for rim formation include condensation, flash heating, and metasomatism (MacPherson et al. 1981; MacPherson and Grossman 1984; Davis et al. 1986; Davis and MacPherson 1994; Krot et al. 1995; Wark and Boynton 2001; MacPherson 2004). Condensation involves direct sublimation of atoms and/or molecules in the (nebular) gas phase to solid mineral grains, either as single crystals or films, onto previously condensed dust. In the metasomatic model, a fluid consisting of either the nebular gas or a parent-body gas/fluid reacts with already condensed CAI material to form surface layers (rims) of varied composition (MacPherson et al. 1981; Ruzicka 1997). In comparison, flash heating involves exposure of a CAI to a thermal pulse, on the order of 1–2 s in duration at temperature above 2000 °C, followed by partial melting and crystallization, and later reaction of the nebular gas with the rim surface (Wark and Boynton 2001). We

hypothesize that flash heating followed by rapid crystallization would almost certainly result in the formation of glass or glassy pockets in the rims. Based on our EBSD and TEM data for the areas of the rims that we have measured, we do not observe glassy material and so infer that flash heating, while a viable origin for other rims, did not play a significant role in the origins of those that we report on here. With respect to rim formation via metasomatic reaction, we note that inner parts of the rims have been reported to contain Ti^{3+} and are FeO-poor (Simon et al. 2007), suggesting that if metasomatism occurred, it was a nebular condensation process rather than parent-body mediated. Thus, for the purposes of the discussion below, we will refer to the process of atoms and/or molecules attaching to and ordering themselves onto the CAI surface as condensation.

Based on the above discussion, we hypothesize that several condensation modes are possible for the oriented grains observed here, and these include (a) condensation entirely from atoms that were in the gas, by nucleating in an oriented way onto a pre-existing phase; (b) formation by reaction between gaseous species and a pre-existing phase to form a new phase on the surface of the pre-existing phase, in an oriented way; (c) a phase that condenses entirely from gas atoms, not nucleating on the surface but which subsequently attaches itself to a pre-existing phase in an oriented way; and (d) an ex situ condensate phase that aligns itself because the grains sediment themselves from a flowing gas or in a gravity field. We rule out scenario (c) because a previously condensed phase would be much more likely to align randomly with the melilite surface during attachment rather than the preferred orientations we observe here. For example, SEM and TEM images of the matrices of several type 3 ordinary and carbonaceous chondrites, which are believed to have formed via condensation, show that grains within them have random orientations (e.g., Huss et al. 1981; Nagahara 1984; Brearley et al. 1989; Cosarinsky et al. 2008), that were presumably acquired during accretion. Scenario (d) also seems unlikely because if the grains had condensed from a flowing gas or gravity field, we would have expected to find crystals with a physical elongation of a major axis in the direction of that flow, which was not observed in this work. Scenarios (a) and (b) however, can both account for rim formation.

In synthetic materials, the use of multistage, seeded-growth methods has led to a wide range of nanostructures, including oriented nanowires, nanotubes, and nanoneedles, as well as multilayer heterostructures (De Mul and Mann 1994; Sounart et al. 2006; and references therein). Multilayer heterostructures, akin to the rims on CAIs, were shown to form layered sequences at free surfaces. In some cases, the individual layers immediately restructured as crystalline multilayer stacks whose development was guided by the underlying lattice, as we hypothesize for rims. These layered stacks contributed to oriented crystal growth by serving as sources of subsequent growth steps. In other cases, microcrystals formed in a discontinuous way on the underlying lattice, and were later incorporated into the growing crystal as defects (Kuznetsov et al. 1998). Analogous mechanisms may have been behind rim formation in scenarios (a) and (b) above.

Analytical studies to resolve excess ^{26}Mg in the low Al/Mg phases characteristic of rims have shown that high-temperature processes occurred hundreds of thousands of years after CAI formation (Simon et al. 2005; Taylor et al. 2005), and Cosarinsky et al. (2005) reports that rim formation could have occurred over a period of $\sim 2 \times 10^5$ yr. The orientations observed in AX30 may be the result of a two-step process, where the melilite inclusion is melted and solidifies into a spherical morphology, followed by condensation to form the rim.

Refractory inclusions in primitive CV chondrites have been shown to contain Fe- and alkali-rich secondary phases resulting from metasomatic alteration (Kimura and Ikeda 1997; Krot et al. 2002) as well as phyllosilicates and other hydrated phases resulting from aqueous processing (Tomeoka and Buseck 1986; Lee and Greenwood 1993). We did not observe sheet silicates or alkali-rich alteration products in either the FIB or thin sections. Iron was observed in the pyroxene in the FIB section of AX30, however, indicating some degree of secondary alteration (e.g., MacPherson and Krot 2014). This process does not seem to have affected the microstructure observed here, and the grain orientations appear to be primary.

Oriented, island-type growth therefore appears to be the mode of pyroxene formation common to the two rims studied here. That part of the anorthite layer is also oriented with respect to the pyroxene suggests that subsequent growth of the overlying layers was likely affected by the orientation(s) of the initial condensing material. Moreover, the DFT calculations indicate that such oriented growth is an energy-minimized process. We note that previous TEM observations revealed clusters of oriented grains within the pyroxene layer of a rim on an inclusion in the Vigarano CV3 chondrite (Zega et al. 2010). Based on the present work and those previous results, we hypothesize that preferred orientation may be a common energy-minimized growth mode for grains within the rims on CV3 inclusions.

CONCLUSIONS

We have carried out a detailed microstructural study of the rims on a CTA from Axtell (AX30) and an FTA from Allende (TS25), both oxidized CV3 chondrites. EBSD and TEM analyses show that grains at the surfaces of the rim assemblages as well as at depth in both samples have preferred orientations. Clusters of pyroxene grains have orientations common to one another in both TS25 and AX30, and an epitaxial relationship exists among grains within diopside and anorthite layers in TS25. We conclude that the microstructure of the rims on TS25 and AX30 is the result of high-temperature condensation of individual grains from a nebular gas, followed by island-type growth into oriented aggregates to form the rim layers. Regardless of the parent-body histories of TS25 or AX30, the oriented growth of the clusters of grains within their rims was preserved. The data suggest that oriented nucleation may be a common growth mode for mineral grains within the rims on inclusions in CV3 chondrites, irrespective of whether the host inclusion formed via condensation or crystallization from a melt as hypothesized, respectively, for FTA and CTA CAIs.

Acknowledgments—We thank Chi Ma, AE Ed Scott, and an anonymous reviewer for comments that helped improve the manuscript. Research was funded by NASA grant NNX12AL47G (TJZ), NNX13AE73G (LG), and NESSF grant NNX14AO56H (DB). We acknowledge use of the FIB and TEM instruments in the John M. Cowley Center for High Resolution Electron Microscopy at Arizona State University and Electron Beam Analysis Labs at the NASA Johnson Space Center.

Editorial Handling—Dr. Edward Scott

REFERENCES

Allen J. M., Grossman L., Davis A. M., and Hutcheon I. D. 1978. Mineralogy, texture, and mode of formation of a hibonite-bearing Allende inclusion. Proceedings, 9th Lunar and Planetary Science Conference. pp. 1209–1233.

Armstrong J. T., Meeker G. P., Hueneke J. C., and Wasserburg G. J. 1982. The Blue Angel: I. The mineralogy and petrogenesis of a hibonite inclusion from the Murchison meteorite. *Geochimica et Cosmochimica Acta* 46:575–595.

Barber D. J., Martin P. M., and Hutcheon I. D. 1984. The microstructure of minerals in coarse-grained Ca-Al-rich inclusions from the Allende meteorite. *Geochimica et Cosmochimica Acta* 48:769–783.

Beckett J. R., Connolly H. C. Jr., and Ebel D. S. 2006. Chemical processes in calcium-aluminum-rich inclusions: A mostly CMAS view of melting and crystallization. In *Meteorites and the early solar system II*, edited by Lauretta D. S. and McSween H. Y. Jr. Tucson, Arizona: The University of Arizona Press. pp. 399–429.

Blander M. and Fuchs L. H. 1975. Calcium-aluminum-rich inclusions in the Allende meteorite: Evidence for a liquid origin. *Geochimica et Cosmochimica Acta* 39:1605–1619.

Blöchl P. E. 1994. Projector augmented-wave method. *Physical Review B* 50:17953.

Brearley A. J., Scot E. R. D., Keil K., Clayton R. N., Mayeda T. K., Boynton W., and Hill D. H. 1989. Chemical, isotopic, and mineralogical evidence for the origin of matrix in ordinary chondrites. *Geochimica et Cosmochimica Acta* 53:2081–2093.

Busemann H., Nguyen A. N., Cody G. D., Kilcoyne A. L. D., Stroud R. M., Zega T. J., and Nittler L. R. 2009. Ultra-primitive interplanetary dust particles from the comet 26P/Grigg-Skjellerup dust stream collection. *Earth and Planetary Science Letters* 288:44–57.

Cosarinsky M., McKeegan K. D., Hutcheon I. D., Weber P., and Fallon S. 2005. Magnesium and oxygen isotopic study of the Wark-Lovering Rim around a fluffy type-A inclusion from Allende (abstract #2105). 36th Lunar and Planetary Science Conference. CD-ROM.

Cosarinsky M., Leshin L., MacPherson G., Guan Y., and Krot A. 2008. Chemical and oxygen isotopic compositions of accretionary rim and matrix olivine in CV chondrites: Constraints on the evolution of nebular dust. *Geochimica et Cosmochimica Acta* 72:1887–1913.

Davis A. M. and MacPherson G. J. 1994. Constraints on the formation of rims on CAIs. *Meteoritics* 29:458–459.

Davis A. M., MacPherson G. J., and Hinton R. W. 1986. Rims revealed-ion microprobe analysis of individual rim layers in a Vigarano type A inclusion. *Meteoritics* 21:349–351.

De Mul M. N. G. and Mann A. J. 1994. Multilayer formation in thin films of thermotropic liquid crystals at the air-water interface. *Langmuir* 10:2311–2316.

Doukhan N., Doukhan J. C., and Poirier J. P. 1991. Transmission electron microscopy of a refractory inclusion from the Allende meteorite: Anatomy of a pyroxene. *Meteoritics* 26:105–109.

Ebel D. S. 2006. Condensation of rocky material in astrophysical environments. In *Meteorites and the early solar system II*, edited by Lauretta D. S. and McSween H. Y. Jr. Tuscon, Arizona: The University of Arizona Press. pp. 253–277.

Ebel D. S. and Grossman L. 2000. Condensation in dust-enriched systems. *Geochimica et Cosmochimica Acta* 64:339–366.

Evans J. W., Thiel P. A., and Bartelt M. C. 2006. Morphological evolution during epitaxial thin film growth: Formation of 2D islands and 3D mounds. *Surface Science Reports* 61:1–128.

Floss C., Le Guillou C., and Brearley A. 2014. Coordinated NanoSIMS and FIB-TEM analyses of organic matter and associated matrix materials in CR3 chondrites. *Geochimica et Cosmochimica Acta* 139:1–25.

Graham G. A., Teslich N. E., Kearsley A. T., Stadermann F. J., Stroud R. M., Dai Z. R., Ishii H. A., Hutcheon I. D., Bajt S., Snead C. J., Weber P. K., and Bradley J. P. 2008. Applied focused ion beam techniques for sample preparation of astromaterials for integrated nanoanalysis. *Meteoritics & Planetary Science* 43:561–569.

Greenwood R. C., Lee M. R., Hutchison R., and Barber D. J. 1994. Formation and alteration of CAIs in Cold Bokkeveld (CM2). *Geochimica et Cosmochimica Acta* 58:1913–1935.

Greshake A., Bischoff A., and Putnis A. 1998. Transmission electron microscope study of compact Type A calcium-aluminum-rich inclusions from CV3 chondrites: Clues to their origin. *Meteoritics & Planetary Science* 33:75–87.

Grossman L. 1972. Condensation in the primitive solar nebula. *Geochimica et Cosmochimica Acta* 36:597–619.

Grossman L. 1975. Petrography and mineral chemistry of Ca-rich inclusions in the Allende meteorite. *Geochimica et Cosmochimica Acta* 39:433–454.

Han J., Brearley A. J., and Keller L. P. 2014. Microstructures of hibonite from an ALHA77307 (CO3.0) CAI: Evidence for evaporative loss of calcium (abstract #5440). 77th Meteoritical Society Meeting.

Han J., Keller L. P., Needham A. W., Messenger S., and Simon J. I. 2015a. Microstructural investigation of a Wark-Lovering rim on a Vigarano CAI (abstract #5243). 78th Meteoritical Society Meeting. *Meteoritics & Planetary Science* 50.

Han J., Brearley A. J., and Keller L. P. 2015b. Microstructural evidence for a disequilibrium condensation origin for hibonite-spinel inclusions in the ALHA77307 CO3.0 chondrite. *Meteoritics & Planetary Science* 50:2121–2136. doi: 10.1111/maps.12563.

Heaney P. J., Vicenzi E. P., Gianuzzi L. A., and Livi K. J. T. 2001. Focused ion beam milling: A method of site-specific sample preparation for microanalysis of Earth and planetary materials. *American Mineralogist* 86:1094–1099.

Huss G. R., Keil K., and Taylor G. J. 1981. The matrices of unequilibrated ordinary chondrites: Implications for the origin and history of chondrites. *Geochimica et Cosmochimica Acta* 45:33–51.

Huss G. R., MacPherson G. J., Davis A. M., Krot A. N., and Ulyanov A. A. 2002. Microdistribution of REE in fine-grained group II CAIs in Efremovka (abstract). *Meteoritics & Planetary Science* 37:A68.

Hwang R. Q. and Bartelt M. C. 1997. Scanning tunneling microscopy studies of metal on metal epitaxy. *Chemical Reviews* 97:1063–1082.

Ireland T. R. 1988. Correlated morphological, chemical, and isotopic characteristics of hibonite from the Murchison carbonaceous chondrite. *Geochimica et Cosmochimica Acta* 52:2827–2839.

Keller L. P. and Buseck P. R. 1991. Calcic micas in the Allende meteorite: Evidence for hydration reactions in the early solar nebula. *Science* 252:946–949.

Keller L. P., Needham A. W., and Messenger S. 2013. A FIB/TEM study of complex Wark-Lovering rim on a Vigarano CAI (abstract 5300). 76th Annual Meteoritical Society Meeting.

Keller L. P., Needham A. W., and Messenger S. 2014. A FIB/TEM/NANOSIMS study of a Wark-Lovering rim on an Allende CAI (abstract #5428). 77th Annual Meteoritical Society Meeting. *Meteoritics & Planetary Science* 49.

Kimura M. and Ikeda Y. 1997. Comparative study of anhydrous alteration of chondrules in reduced and oxidized CV chondrites. *Antarctic Meteorite Research* 10:191–202.

Kornacki A. and Wood J. A. 1984. Petrography and classification of Ca, Al-rich and Olivine-rich inclusions in the Allende CV3 chondrite. *Journal of Geophysical Research* 89:B573–587.

Kresse G. and Furthmuller J. 1996. Efficiency of ab-initio total energy calculation for metals and semiconductors using plane-wave basis set. *Computational Materials Science* 6:15–50.

Kresse G. and Joubert D. 1999. From ultrasoft pseudopotentials to the projector augmented-wave method. *Physical Review B* 59:1758–1775.

Krot A. N., Scott E. R. D., and Zolensky M. E. 1995. Mineralogical and chemical modification of components in CV3 chondrites: Nebular or asteroidal processing? *Meteoritics* 30:748–775.

Krot A. N., Hutcheon I. D., and Keil K. 2002. Plagioclase-rich chondrules in the reduced CV chondrites: Evidence for complex formation history and genetic links between calcium-aluminum-rich-inclusions and ferromagnesian chondrules. *Meteoritics & Planetary Science* 37:155–182.

Krot A. N., MacPherson G. J., Ulyanov A. A., and Petaev M. I. 2004. Fine-grained, spinel-rich inclusions from the reduced CV chondrites Efremovka and Leoville: I. Mineralogy, petrology, and bulk chemistry. *Meteoritics & Planetary Science* 39:1517–1553.

Kuznetsov Y. G., Malkin A. J., and McPherson A. 1998. Atomic-force-microscopy studies of phase separations in macromolecular systems. *Physical Review B* 58:6097.

Lee M. R. and Greenwood R. C. 1993. Alteration of calcium- and aluminum-rich inclusions in the Murray (CM2) carbonaceous chondrite. *Meteoritics* 29:780–790.

Lee M. R., Bland P. A., and Graham G. 2003. Preparation of TEM samples by focused ion beam (FIB) techniques: Applications to the study of clays and phyllosilicates in meteorites. *Mineralogical Magazine* 67:581–592.

Lodders K. 2003. Solar system abundances and condensation temperatures of the elements. *The Astrophysical Journal* 591:1220–1247.

Ma C., Kampf A. R., Connolly H. C. Jr, Beckett J. R., Rossman G. R., Sweeney Smith S. A., and Schrader D. L. 2011. Krotite, $CaAl_2O_4$, a new refractory mineral from the NWA 1934 meteorite. *American Mineralogist* 96:709–715.

MacPherson G. J. 2004. Calcium-aluminum-rich inclusions in chondritic meteorites. In *Meteorites*, edited by Davis A. M. Treatise on Geochemistry, vol. 1. Oxford: Elsevier Ltd. pp. 201–246.

MacPherson G. J. and Grossman L. 1979. Melted and non-melted coarse-grained Ca-, Al-rich inclusions in Allende. *Meteoritics* 14:479–480.

MacPherson G. J. and Grossman L. 1984. "Fluffy" type A Ca-, Al-rich inclusions in the Allende meteorite. *Geochimica et Cosmochimica Acta* 48:29–46.

MacPherson G. J. and Krot A. N. 2014. The formation of Ca-, Fe-rich silicates in reduced and oxidized CV chondrites: The roles of impact-modified porosity and permeability, and heterogeneous distribution of water ices. *Meteoritics & Planetary Science* 49:1250–1270.

MacPherson G. J., Grossman L., Allen J. M., and Beckett J. R. 1981. Origin of rims on coarse-grained inclusions in the Allende meteorite. Proceedings, 12th Lunar and Planetary Science Conference. *Geochimica et Cosmochimica Acta* 2:1079–1091.

MacPherson G. J., Bar-Matthews M., Tanaka T., Olsen E., and Grossman L. 1983. Refractory inclusions in the Murchison meteorite. *Geochimica et Cosmochimica Acta* 47:823–839.

Maranville B. B., Schuerman M., and Hellman F. 2006. Simulation of clustering and anisotropy due to Co step-edge segregation in vapor-deposited $CoPt_3$. *Physical Review B* 73:104435.

McSween H. Y. 1977. Petrographic variations among carbonaceous chondrites of the Vigarano type. *Geochimica et Cosmochimica Acta* 41:1777–1790.

Muller W. F. and Wlotzka F. 1982. Mineralogical study of the Leoville meteorite (CV3): Macroscopic texture and transmission electron microscopic observations (abstract). 13th Lunar and Planetary Science Conference. p. 558.

Nagahara N. 1984. Matrices of type 3 ordinary chondrites—Primitive nebular records. *Geochimica et Cosmochimica Acta* 48:2581–2595.

Nguyen A. N., Nittler L. R., Stadermann F. J., Stroud R. M., and Alexander C. M. O'D. 2010. Coordinated analyses of presolar grains in the Allan Hills 77307 and Queen Elizabeth Range 99177 meteorites. *The Astrophysical Journal* 719:166–189.

Paque J. M., Beckett J. R., Ishii H. A., Aleon-Toppani A., Burnett D. S., Teslich N., Dai Z. R., and Bradley J. P. 2009. The formation of boundary clinopyroxenes and associated glass veins in type B1 CAIs. *Meteoritics & Planetary Science* 44:665–687.

Parker S. C., Grant A. W., Bondzie V. A., and Campbell C. T. 1999. Island growth kinetics during the vapor deposition of gold onto TiO_2(110). *Surface Science* 441:10–20.

Perdew J. P., Burke K., and Ernzerhof M. 1996. Generalized gradient approximation made simple. *Physical Review Letters* 77:3865–3868.

Ruzicka A. 1997. Mineral layers around coarse-grained, Ca-Al-rich inclusions in CV3 carbonaceous chondrites: Formation by high-temperature metasomatism. *Journal of Geophysical Research: Planets* 102:13,387–13,402.

Shchukin V. A. and Bimberg D. 1999. Spontaneous ordering of nanostructures on crystal surfaces. *Reviews of Modern Physics* 71:1125.

Simon S. B., Yoneda S., Grossman L., and Davis A. M. 1994. A $CaAl_4O_7$-bearing refractory spherule from Murchison: Evidence for very high-temperature melting in the solar nebula. *Geochimica et Cosmochimica Acta* 58:1937–1949.

Simon S. B., Davis A. M., and Grossman L. 1999. Origin of compact type A refractory inclusions from CV3 carbonaceous chondrites. *Geochimica et Cosmochimica Acta* 63:1233–1248.

Simon S. B., Sutton S. R., and Grossman L. 2007. Valence of titanium and vanadium in pyroxene in refractory inclusions and rims. *Geochimica et Cosmochimica Acta* 71:3098–3118.

Simon J. I., Young E. D., Russell S. S., Tonui E. K., Dyl K. A., and Manning C. E. 2005. A short timescale for changing oxygen fugacity in the solar nebula revealed by high-resolution ^{26}Al-^{26}Mg dating of CAI rims. *Earth and Planetary Science Letters* 238:272–283.

Sounart T. L., Liu J., Voigt J. A., Hsu J. W. P., Spoerke E. D., Tian Z., and Jiang Y. B. 2006. Sequential nucleation and growth of complex nanostructured films. *Advanced Functional Materials* 16:335–344.

Stolper E. and Paque J. M. 1986. Crystallization sequences of Ca-Al-rich inclusions from Allende; the effects of cooling rate and maximum temperature. *Geochimica et Cosmochimica Acta* 50:1785–1806.

Stroud R. M., Alexander C. M. O'D., and MacPherson G. J. 2000. A precise new method of microsampling chondritic material for transmission electron micro-scope analysis: Preliminary application to calcium-aluminium-rich inclusions and associated matrix material in the Vigarano CV3 meteorite. *Meteoritics & Planetary Science Supplement* 35:A153–154.

Stroud R. M., Nittler L. R., and Alexander C. M. O'D. 2004. Polymorphism in presolar Al_2O_3 grains from asymptotic giant branch stars. *Science* 305:1455–1457.

Taylor D. J., McKeegan K. D., and Krot A. N. 2005. High resolution 26Al chronology: Resolved time interval between rim and interior of a highly fractionated compact type A CAI from Efremovka (abstract #2121). 36th Lunar and Planetary Science Conference. CD-ROM.

Tomeoka K. and Buseck P. R. 1986. Phyllosilicates in the Mokoia CV3 carbonaceous chondrite: Petrographic and transmission electron microscope observations (abstract). 17th Lunar and Planetary Science Conference. p. 899.

Toppani A., Libourel G., Robert F., and Ghanbaja J. 2006. Laboratory condensation of refractory dust in protosolar and circumstellar conditions. *Geochimica et Cosmochimica Acta* 70:5035–5060.

Wark D. A. and Boynton W. V. 2001. The formation of rims on calcium-aluminum-rich inclusions: Step I—Flash heating. *Meteoritics & Planetary Science* 36:1135–1166.

Wark D. A. and Lovering J. F. 1977. Marker events in the early solar system: Evidence from rims on Ca-Al-rich inclusions in carbonaceous chondrites. Proceedings, 8th Lunar Science Conference. pp. 95–112.

Zega T. J., Nittler L. R., Busemann H., Hoppe P., and Stroud R. M. 2007a. Coordinated isotopic and mineralogic analyses of planetary materials enabled by in situ lift-out with a focused ion beam scanning electron microscope. *Meteoritics & Planetary Science* 42:1373–1386.

Zega T. J., Cosarinsky M., Stroud R. M., and McKeegan K. D. 2007b. FIB-TEM study of a Wark-Lovering rim in an Allende type A CAI. *Meteoritics & Planetary Science* 42: A169.

Zega T. J., Cosarinsky M., MacPherson G. J., and McKeegan K. D. 2009. FIB-TEM analysis on a Wark-Lovering rim from the Vigarano CV3 chondrite. *Meteoritics & Planetary Science* 44:A226.

Zega T. J., Simon S. B., and Grossman L. 2010. Microstructural analysis of a Wark-Lovering rim around an Allende CAI. *Meteoritics & Planetary Science* 45:A223.

Zega T. J., Nittler L. R., Gyngard F., Alexander C. M. O'D., Stroud R. M., and Zinner E. K. 2014. A transmission electron microcopy study of presolar spinel. *Geochimica et Cosmochimica Acta* 124:152–169.